DFT Calculation, Molecular Docking and Molecular Dynamics Simulation Study on Substituted Phenylacetamide and Benzohydrazide Derivatives

Vidyasrilekha Yele
JSS College of Pharmacy Ooty
Dilep Kumar Sigalapalli
Vignan Pharmacy College
Srikanth Jupudi
JSS College of Pharmacy Ooty
Mohammed Afzal Azam (afzal9azam@hotmail.com)
JSS College of Pharmacy https://orcid.org/0000-0001-9770-9371

Research Article

Keywords: DFT, Bond dissociation energy, Binding free energy, Molecular dynamic simulation, Phenylacetamides and benzohydrazides

Posted Date: August 18th, 2021

DOI: https://doi.org/10.21203/rs.3.rs-779643/v1

Version of Record: A version of this preprint was published at Journal of Molecular Modeling on November 24th, 2021. See the published version at https://doi.org/10.1007/s00894-021-04987-8.

Abstract

The atomic and molecular properties of the title compounds were calculated by Jaguar using a basis set B3LYP/6-31G**++ with hybrid DFT in the gas phase, to determine the chemical reactivity. Analysis of Quantum chemical features such as HOMO and LUMO explained that the electronic charge transfer occurred within the system through conjugated paths of the selected compounds. The nucleophilic and electrophilic reactive sites are recognized from the molecular electrostatic potential plot. Electrophilic and nucleophilic attack-prone molecular sites were predicted by mapping ALIE and ALEA values to the molecular surface. The bond dissociation energy of the high active compound **15** (2-chloro-N-(2-(2-(2-(2-chlorobenzoyl)hydrazineyl)-2-oxoethoxy)phenyl)acetamide) was calculated to assess the probability of compounds autoxidation or degradation. Further, molecular docking, binding free energy calculations, and ADMET profile of the degradation products (DPs) of compound **15** was carried out to determine the binding affinity and toxicity profile of the formed DPs compared with the parent compound. A 150 ns molecular dynamics (MD) simulation was performed to evaluate the binding stability of the compound **15**/4URL complex using Desmond. Binding free energy and binding affinity of the complex were computed for 100 trajectory frames using the MM-GBSA approach.

1. Introduction

Antibacterial resistance (ABR) is a rising global burden, threatening our ability to treat common infectious diseases [1, 2]. As per the statistics by the center for disease control and prevention report 2019, 15 more antibiotic-resistant strains were discovered and classified as ‘urgent’, ‘serious’, and ‘concerning’ threats. This demands the discovery of small-molecule inhibitors to overwhelm ABR. Consequently, various strategies have emerged to develop new molecules that could either act as drugs or by adjoining the different bioactive moieties that are known to possess biological activity against nosocomial pathogens [3–7].

In the recent past, phenylacetamides [8, 9] and benzohydrazides [10–12] have garnered attention among researchers, especially in the discovery and synthesis of novel compounds with notable biological activities. These moieties contain active amide and hydrazide fragments that act as links between any aryl or heteroaryl groups. Due to their intensive pharmacological activity, these are widely used in organic synthesis. Phenylacetamides [13, 14] and benzohydrazides [15] find application in designing and developing novel drugs that are known to possess antitubercular, antimicrobial, antimalarial [12] and anti-inflammatory [16] properties. Phenylacetamides and benzohydrazides with electron-withdrawing and donating groups provide a pathway for redistribution of electron density under the influence of the external field. Such compounds are of utmost importance in material chemistry. Their strong chemical stability serves as an attractive future material in different areas such as optoelectronics technologies, optical switching device, and chemo sensors development.

Pharmaceutically, organic molecules are the candidates that are synthesized to be stable in the aquatic environment. Regrettably, a typical environment is not appropriate for the degradation of the organic compounds in water, which led to their accretion in all types of water worldwide [17–19]. Hence, the stability and reactivity of the molecules command the fate of the pharmaceutical ingredient in the environment [20].

However, forced degradation methods are performed to enhance the degradation techniques of active ingredients in the formulation [21]. Moreover, these studies are of great importance from the aspect of desirable resources; thus, the computational tools are employed for optimization and rationalization of such experiments [20, 22, 23]. Density functional theory (DFT), *Ab initio*, Semi-empirical Self-consistent Field (SCF), and Molecular mechanics approaches serve as the crucial tools of computational chemistry. In addition, DFT was used to calculate model structures such as Fluorinated Ethylene Propylene (Teflon FEP), polymethyl methacrylate Kapton polyimiide (Fig. 1)

Further, specific correlations among different components are readily computed by *in silico* approaches from one side and the physicochemical properties from the other aspect. One example is bond dissociation energies (BDE) of DFT calculations which can be employed for the molecule site prediction where autoxidation might occur. The degradation products (DPs) formed during storage are the latent source for toxicity, which plays a crucial role in drug discovery and development. Thus, the characterization and toxicity evaluation of predicted DPs may provide support to lessen the adverse effects and avoid the recall of drugs from the market [24].

Moreover, quantum chemical calculations are reasonably necessary to understand electronic polarization, responsible for predicting novel properties and non-linearity. The non-linearity of the compound can be synthetically modeled by extending the π-conjugated system or by optimizing donor-acceptor strength. The effect of water and hydrolysis of tested molecules can be evaluated by molecular dynamic (MD) simulations and radial distribution function calculations.

Thus, considering the importance of phenylacetamides and benzohydrazides from the pharmaceutical aspect, we employed DFT calculations and MD simulations to anticipate some significant reactive properties. In our earlier studies, we reported the synthesis and antibacterial activities of phenylacetamides and benzohydrazides [25, 26] (Supplementary Table 1). Here we report the DFT calculations and MD simulation studies on the above-mentioned molecules in continuation of the above work.

2. Materials And Methods

2.1. DFT-calculations and electrostatic potential (ESP) calculations

All atomic and molecular properties of the compounds were calculated by Jaguar (v8.8, Schrödinger 2019-2) using a basis set 6-31G^{**++} with hybrid DFT of Hamiltonian-nonrelativistic correlation function (B3LYP) in the gas phase (Table 1). DFT energetics demonstrates 3D electronic states of molecules to evaluate the transfer of lone pairs, bonds, and reactivity in a specific environment [27]. Further, selected ligands were examined for their quantum chemical features, such as localization energies of lowest unoccupied molecular orbital (LUMO) and highest occupied molecular orbital (HOMO) and molecular electrostatic potential (MESP) using Jaguar [28]. These localization energies are named frontier molecular orbitals (FMOs) that display a crucial role in maintaining chemical stability and are also used as an efficient tool for investigating donor-acceptor interactions [29]. HOMO characterizes the ligand's ability to donate an electron, whereas LUMO refers to the ability of the ligand to accept an electron. Low values of LUMO indicate the higher propensity of the molecule to accept electrons, whereas higher values of HOMO dictate the increased propensity to donate electrons to unoccupied molecular orbitals. The values of HOMO, LUMO, and their energy gap reproduce the level of conductivity, reactivity, and kinetic stability of the compound. In soft molecules, electron transfer from HOMO to LUMO with low kinetic stability and high chemical reactivity is more effortless if the value of the energy gap is small, which influences the biological activity. The higher energy gap between HOMO and LUMO indicates the kinetic instability of molecule, whereas, narrow HOMO and LUMO energy gap enables intra-molecular charge transfer, making the compound's non-linear optical (NLO) properties active [30, 31]. Structural geometry of ligand was optimized at B3LYP/6-31G^{**++} level, and energy calculation was performed with Poisson Boltzmann Finite (PBF) solvation state [32]. The DFT energy of a system is calculated as

$E_{DFT}=E_{NN}+E_{ET}+E_{V}+E_{COUL}\ E_{EXCH}+E_{CORR}$

E_{NN}: nuclear-nuclear repulsion; E_{COUL}: electron-electron coulomb repulsion; E_{V}: nuclear electron attraction; E_{ET}: kinetic energy; E_{CORR}: correlated movement of electrons with different spin and E_{EXCH}: electron-electron exchange energy.

MESP demonstrates the electron density distribution around the molecule and also predicts the molecules chemical reactivity. MESP is a tool for predicting chemical reactivity where negative potential regions (protonation sites) involve in

the nucleophilic attack, whereas positive potential regions is susceptible for electrophilic attack. DFT energy and MESP knowledge are mainly employed to predict possible functional spots in ligands for potential interactions with the residues of the target. Moreover, potential molecules were evaluated in terms of the HOMO and LUMO energy gap [33].

2.2. Bond dissociation energy

Further, Bond dissociation energy (BDE) of the high active molecule was performed using Materials Science suite (Schrödinger 2019-2). Geometry optimization was performed without considering any constraints using hybrid density functional B3LYP with 6-31G^{**++} basis set.

2.3. Molecular docking and Binding free energy calculations

Docking studies were performed in extra-precision (XP) mode [34] for compound **15** and its probable degradation products (DPs)/BDE fragments using Glide module (Schrödinger 2019-2) without applying any constraints. The crystal structure of *S. aureus* ParE enzyme complexed with keibdelomycin (PDB ID: 4URL, resolution 1.9 Å) was retrieved from the RCSB-PDB and then prepared using the Protein Preparation Wizard module. Ionization states of amino acid residues at pH 7.0 were generated, and hydrogen atoms were added to the protein. Missing side chains or loops were filled using the module Prime [35]. Energy minimization and optimization were performed using the OPLS3e force field [36] with root mean square deviation (RMSD) at 0.30 Å. In this study, a glide grid was created at the centroid of the co-crystal ligand keeping the partial charge cut-off at 0.25 and van der Waals scaling of 1.0 for the receptor. Compound **15** and its DPs were optimized using the LigPrep module to generate low energy conformers.

Binding free energy calculations of selected ligands were calculated using the Prime, MM-GBSA approach. The energy calculations of protein-ligand complexes were performed using the continuum solvent (VSGB 2.0) model [37] and OPLS3e force field.

2.4. Prediction of pharmacological and toxicological properties

In recent years, the significance of favorable pharmacokinetic features for discovering successful drug candidates has been widely acknowledged. Thus, ADMET evaluations are integrated earlier into the field of drug design and discovery. QikProp [38] proved to be a novel tool in computing and optimizing the pharmacokinetic profile or ADMET relevant descriptors for pharmaceutically acceptable compounds. Further, this algorithm is also used to correlate physicochemical and pharmacokinetic properties with the 3D molecular structure of the test ligands. Neutralization of compounds is an essential step that is performed before being used by QikProp, as this tool is incapable of neutralizing a compound. A total of 44 predicted properties such as physicochemical properties, principal descriptors, LogP, QP%, and log HERG are generated in normal mode. It also determines the acceptability of the ligands, based on Lipinski's rule of five [39] and three, which are crucial for rational drug design.

2.5. Molecular dynamics simulation and analysis

MD simulations were performed of the docked complex **15**/4URL using the OPLS3e force field [35]. The system was solvated in an orthorhombic boundary box with explicit TIP4P water within the Desmond MD system [40, 41]. Counter ions were added to achieve the neutralization of the system. The system comprises 50390 atoms and 14800 water molecules. System minimization was carried out with OPLS3e force field using 200 steepest descent algorithms, followed by 1000 conjugate gradient steps until a gradient threshold of 25 kcal/mol reached. The Smooth Particle Mesh Ewald method was employed for short-range van der Waals and coulomb interactions at a cut-off radius of 9 Å, while tolerance of 1e-09 was applied for the long-range electrostatic interactions [42]. A 150 ns MD simulation was performed under isobaric and isothermal ensemble (NPT) with a pressure of 1 bar and temperature of 300 K using Martyna-Tobias Klein and Noose-Hoover thermostat methods, respectively [43, 44]. REPSA integration algorithm [45] was employed for the bonded, near, and far non-bonded interactions with multiple time steps of 2, 2, 6 fs, respectively. Maestro graphical user interface was

used to visualize the trajectories and 3D structures. Further, binding free energy calculation of **15**/4URL complex was carried out using the MM-GBSA approach

3. Results And Discussion

The atomic and molecular properties of the title compounds were calculated using Jaguar (Schrödinger 2019-2) using a basis set 6-31G**$^{++}$ with hybrid DFT with Hamiltonian-nonrelativistic correlation function (B3LYP) in the gas phase, and the results are summarized in Table 1. In this article we discussed DFT calculations, bond dissociation energies mainly focusing on compound **15** which considered to be highly active among the tested compounds.

3.1. Frontier molecular orbital analysis

The frontier molecular orbital analysis demonstrates the intramolecular charge transfer between the acceptor and donor functional groups through the conjugated paths [46]. In the current study the HOMO and LUMO energies are in the range of 9.57319 to 4.58334 eV and 2.19099 to 0.12709 eV, respectively. The HOMO of the high active compound **15** (MIC, 0.62 µg/ml) is localized at -9.060094 eV, while the LUMO is localized at -5.585780 eV, and there is a charge transfer in the molecular system through the conjugated paths. The energy gap (ΔE) of -3.474314 eV between HOMO and LUMO specifies the molecular chemical stability (Fig. 2). Moreover, the ΔE values showed good correlation (R^2 = 0.812) with the MIC of compounds **1–29** (0.68–8.99 µg/ml) against *Staphylococcus aureus* (NCIM 5022).

Table 1: Atomic and molecular properties of compounds **1-29**

Compound	[a]HOF	[b]HOMO	[c]LUMO	[d]ME	[e]MH	[f]TES	[g]TNS	[h]TESPV	[i]TAV	[j]TAE
1	-68.37	-9.43	-1.22	-5.32	4.10	-6.91	-31.27	0.35	4460.82	474.83
2	-67.36	-8.80	-0.28	-4.54	4.26	-6.54	-20.27	0.19	3812.91	2294.03
3	-174.50	-4.71	1.18	-1.76	2.95	-9.24	-18.34	2.31	6490.41	425.77
4	-73.47	-9.04	-1.21	-5.12	3.91	-7.22	170.62	0.31	4313.71	2284.43
5	-169.18	-4.91	1.23	-1.83	3.07	-9.72	-19.19	2.14	7494.35	1527.23
6	-217.20	-6.13	1.12	-2.50	3.63	-9.77	-19.19	2.12	6916.98	573.9
7	-72.72	-9.25	-2.02	-5.63	3.61	-7.73	20.38	0.32	4790.24	1851.07
8	-190.91	-5.21	1.26	-1.97	3.23	-10.02	-20.90	1.88	6304.55	305.04
9	-60.92	-8.85	-0.26	-4.55	4.29	-6.11	-34.08	0.2	3874.94	375
10	-67.77	-8.99	-0.28	-4.63	4.35	-6.55	-3.27	0.2	3787.14	545.33
11	-77.25	-8.88	-0.58	-4.73	4.15	-7.43	-0.92	0.2	3750.83	356.44
12	-79.90	-8.97	-0.63	-4.80	4.16	-7.27	487.42	0.21	4043.94	351.26
13	-108.21	-8.79	-0.60	-4.69	4.09	-7.58	-7.62	0.18	3860.28	476.14
14	-76.77	-9.07	-1.78	-5.43	3.64	-7.80	73.36	0.28	4429.11	467.13
15	-76.48	-9.06	-5.58	-4.80	4.23	-7.45	-131.32	0.2	3965.86	401.89
16	-61.71	-8.92	-1.00	-4.96	3.96	-7.04	-35.71	0.22	3955.41	513.86
17	-46.53	-9.24	-1.82	-5.53	3.71	-8.08	5.61	0.35	4462.00	659.72
18	-186.97	-5.62	2.19	-1.71	3.91	-9.92	-15.70	1.23	5066.62	269.81
19	30.60	-9.12	-1.17	-5.14	3.97	-6.72	-65.69	0.18	5116.24	2178.08
20	2.391	-9.05	-1.12	-5.08	3.96	-7.04	-128.76	0.17	5115.6	301.54
21	33.18	-9.27	-1.61	-5.44	3.82	-7.25	35.74	0.25	5645.32	364.37
22	-18.19	-8.89	-0.72	-4.81	4.08	-6.64	17.40	0.2	4121.02	587.54
23	51.70	-8.91	-1.23	-5.07	3.84	-5.59	63.26	0.16	5271.91	526.75
24	46.04	-9.57	-1.62	-5.60	3.97	-6.38	-25.28	0.33	5814.62	593.45
25	-72.81	-5.14	0.25	-2.44	2.69	-9.43	-35.08	2.09	7005.91	553.48
26	50.50	-9.24	-1.25	-5.25	3.99	-6.47	1.49	0.23	5575.52	554.37
27	-168.99	-4.58	1.41	-1.58	2.99	-8.17	-14.92	2.66	6092.53	259.48
28	-61.49	-8.71	-0.12	-4.41	4.29	-5.55	90.41	0.16	3611.65	3061.16
29	-7.20	-8.81	-0.66	-4.73	4.07	-6.00	-9.72	0.18	3869.27	614.94

[a]HOF: Heat of formation; [b]HOMO: Highest occupied molecular orbital energy; [c]LUMO: Lowest unoccupied molecular orbital energy; [d]ME: Molecular negativity; [e]MH: Molecular hardness; [f]TES: Total electrophilic super delocalizability; [g]TNS: Total nucleophilic super delocalizability; [h]TESPV: Total ESP variance on molecular surface; [i]TAV: Total ALIE variance on molecular surface; [j]TAE: Total ALEA variance on molecular surface.

3.2. Molecular properties

Electronegativity is a measure of the propensity of an atom to attract electrons in a chemical bond or negative chemical potential of an atom. In contrast, chemical hardness is a measure of resistance to charge transfer. The electrophilicity index of a system demonstrates the energy stabilization and electron affinity and measures the binding energy decay resulting from electron flow between a donor and an acceptor. The molecular electronegativity and hardness of the selected compounds were found to be in the range of -5.601 to -1.586 a.u. and 4.3256 to 2.699 a.u, respectively (Table 1). However, the high active compound **15** exhibited maximum value of electronegativity (-4.802 a.u.) and hardness (4.234 eV).

Moreover, the reactivity of the carbonyl group of a molecule can be explained by the total nucleophilic super delocalizability (TNS) of the carbonyl group, whereas reactivity of olefinic double bond is measured by electrophilic total super delocalizability (TES) [47]. From Table 1, it is evident that the TNS (TNS, -131.326) is more significant than TES (-7.454) of olefinic double bond. This implies that carbonyl group of compound **15** behaves as a nucleophile rather than an electrophile [47].

Molecular electrostatic potential (MESP) is an essential property for predicting and analyzing the molecular reactivity behavior [48] of selected ligands. MESP was computed for compound **15** (Table 1) to indicate the relative reactivity sites for the nucleophilic or electrophilic attack, hydrogen bonding interactions, crystal behavior, macroscopic properties. The positive (light blue) and negative (red) regions in the MESP plot (Fig. 3a) indicates nucleophilic and electrophilic reactivity, respectively. The high active compound **15** exhibited several possible sites of both electrophilic and nucleophilic attack. However, negative ESP points were mainly localized over the carbonyl oxygen and electron cloud of the phenyl ring and the value was found to be 0.07 a.u. on the molecular surface. The deepest positive ESP is localized on the nitrogen and hydrogen atoms with + 0.52 a.u. All these sites indicated the possible strong intermolecular and intramolecular interactions in the crystal lattice.Further, identifying molecular sites prone to electrophilic attacks is of utmost importance for the overall understanding of the molecule's reactivity. ALIE is the energy needed to remove an electron from a specific point or in the space of the system. Average local ionization energy (ALIE) and average local electron affinity (ALEA) surfaces were generated [49] to determine the molecular sites where electrons are loosely bound and tightly bound. Analysis of ALIE of the high active compound **15** explained that carbonyl oxygen atoms are the locations of the loosely bound electrons and hence favorable for the electrophilic reaction or radical attack (Fig. 3b). The high value of ALEA indicated the increased susceptibility of nucleophilic interactions. Analysis of ALEA of compound **15** (Fig. 3c) demonstrated that the region around the phenyl rings and the chlorine atom is highly susceptible to aromatic nucleophilic substitution or addition reactions.

3.3. Bond Dissociation Energy (BDE) of compound 15

For the higher BDE of compound more energy is required for the bond cleavage and vice versa.. A total of 16 DPs were formed for compound **15** by 8 dissociation patterns. The results show that compound **15** exhibited low BDE for DP1a and DP1b (Fig. 4), and the value was found to be 46.161 kcal/mol. In contrast, a high BDE of 85.406 kcal/mol was observed for the DP8a and DP8b.

3.4. Molecular docking and binding free energy calculations of compound 15 and its DPs

XP-docking and the free energy calculations were performed for compound **15** and its DPs against *S. aureus* ParE enzyme to determine the hydrogen-bonding, hydrophobic, π- π and π-cation interactions mainly with N-terminal domain residues. Results are depicted in supplementary Table S2. The docking results have shown significant interactions of compound **15** and its DPs with *S. aureus* ParE (PDB ID: 4URL) (Supplementary Figure S1). The compound **15** exhibited three hydrogen

bonding interactions with Glu53, Gly80 and Thr168. Additionally, this compound was stabilized by π-π stacking interaction of phenyl ring linked to the acetamide fragment with the phenyl ring of Phe106. Further, a π-cation interaction was observed between the same phenyl ring of compound with the protonated NH_2 of Arg79 (Fig. 5). The glide scores for DPs were observed to be in the range of -5.011 to 4.001 kcal/mol.

Prime based MM-GBSA result indicated high binding affinity within the key binding pocket residues of ParE enzyme. The calculated ΔG_{bind} values were found to be in the range of -63.51 to -12.44 kcal/mol. Further, hydrophobic energy (ΔG_{lipo}: -19.88 to -7.65 kcal/mol) term was found to be favorable for the binding of the ligands with ParE protein. Coulomb (ΔG_{cou}: -17.03 to 34.44 kcal/mol) and covalent energy (ΔG_{cov}: -0.60 to 19.86 kcal/mol) terms were observed to be moderately unfavorable for the binding.

3.5. Pharmacological and Toxicological Parameters

The ADMET results obtained through QikProp is represented in supplementary Table S3. ADMET properties of compound **15** and its DPs were found to be in the recommended range. The analysis of the results demonstrated the similarity in the ADMET profile of compound **15** and its DPs. The results exhibited that compound **15** and its DPs possess druggable properties and obeyed the Lipinski rule of five with 0 to 1 violation. The predicted CNS activity of compound **15** and its DPs was found to be in the range of (+ 2 as active and − 2 as inactive), exmplifying a lack of CNS effect. Partition coefficient ($QPlog_{O/W}$) of compound **15** and its DPS (0.2020 to 3.498) is well within the recommended range. Besides, the predicted apparent Caco-2 cell permeability of compound **15** and its DPs was found to be in the range of 162.774 to 1449.673 nm/sec, indicating the high active permeability of these compounds. Solvent accessible surface area (SASA) of compound **15** and its DPs were also observed to be in the recommended range (357.577 to 699.599 $Å^2$). Compound **15** possesses greater SASA (699.599 $Å^2$), indicating the burrial of this compound within the binding pocket compared to its DPs. Compound **15** and its DPs did not exhibit blockadge of HERG K^+ (-2.964 to -3.409) indicating the safety of this compound. Moreover, the polar surface area (PSA) of compound **15** and its DPs were found to be in the range of 56.161 to 120.338 $Å^2$ which is within the recommended range (7-200 $Å^2$), which shows better van der Waal surface area around these molecules.

Further, compound **15** and its DPs possess greater topological surface area (TSA) within the recommended range (< 120 $Å^2$), which indicates the total sum of overall polar atoms or molecules (primarily oxygen and nitrogen, including their attached hydrogen atoms). The compound **15** and its DPs exhibited non-permeability through the blood-brain barrier and are not substrates for P-gp. Further, these are not considered as cytochrome P450. LogKp is a skin permeation indicator showing the compound absorption through the skin. The compound **15** and its DPs possess good permeation through the skin (-6.58 to -7.88 cm/s). However, all DPs possess a bioavailability score (0.55) similar to that of the parent compound. Additionally, compounds exhibited zero Pains alert (PA) (PAN assay interference compounds), indicating the specific interaction with desired target and no interaction with other biological targets.

3.6. Molecular Dynamics Simulation and Analysis

The molecular flexibility, structural behavior, and stability of ParE docked with high active compound **15** was assessed by 150 ns of MD simulation using Desmond. The root mean square deviation (RMSD) values of protein Cα backbone, and heavy atoms increased sharply up to 36 ns and then stabilized in the narrow range of 2.53–3.90 Å, 2.54–3.90 Å and 2.98–4.09 Å, respectively during rest of the simulation time (Fig. 6a). This indicated less fluctuations in protein structure during MD simulation.

The ligand root mean square fluctuation (RMSF) values of Cα atoms, backbone, and heavy atoms of catalytic pocket binding residues were found to be in the range of 0.64–3.01 Å, 0.65–2.90 Å, and 0.76–2.90 Å (Fig. 6b). The maximum RMSF was observed for Phe106 and Lys112 from N-terminal domain present in the loop ranging from Val99 to Gly121,

connecting two α-helices Val122 to Ala127 and Val93 to Thr98. The residues contacting to ligand were observed between Ile46 and Val170 due to pronounce effect of catalytic activity in this region. Whereas no contacts were found in the region between Thr171 and Arg399.

Further, the MD trajectory of **15**/4URL protein complex revealed hydrogen bonding interactions mainly with the polar and charged residues of N-terminal domain dominated by hydrophilic residues. Among the four hydrogen bonds observed in XP-docking, only one (Glu53) was preserved during MD simulations. This may be due to the evolution of inhibitor during MD simulation. Interactions were observed with residues stretching between Ile46 to Val170 (Fig. 6c and 7). However, no π-π stacking, π-cation, and ionic interactions were observed during 150 ns MD simulation. A total of 8 hydrogen bonding interactions were observed, out of which Gly104 formed two strong hydrogen bonds with the nitrogen of phenylacetamide (> C = O···HN, 77% of MD trajectory) and the carbonyl oxygen of hydrazide linker (HN···O = C<, 76% of MD trajectory). Precisely, carbonyl moiety of phenylacetamide formed a strong hydrogen bonding interaction with Thr92 via a water bridge (> C = O···H···O(H)···HN, 66% of MD trajectory). The two NH of hydrazide linker established low frequency hydrogen bonding interaction with Asp52 (18% of MD trajectory) and a moderate frequency hydrogen bonding with Asn49 (38% of MD trajectory) *via* water bridge. In addition, the carbonyl group of hydrazide linker accepted a water-mediated hydrogen bonding interaction with Asp76 (> C = O···H···O(H)···HN, 22% of MD trajectory).

Additionally, ligand also exhibited low-frequency hydrogen bonding interactions with Glu53, Asp76, Arg79, Met81, Pro82, Ile96, and Phe106 (17–19% of the MD trajectory). However, π-π stacking and π-cation interactions were not observed for this compound. It is evident from Supplementary Figure S2 that the phenyl ring of the phenoxy moiety is buried between hydrophobic residues, whereas hydrazide linker and polar fragment (-NH-C = O-CH_2-Cl) present at position two of the phenyl ring of the phenoxy moiety is completely embedded within the hydrophilic residues of the catalytic pocket. It is also evident from the above result that Gly104, Thr92, Asn49, and Asp52 played a crucial role in stabilizing compound **15** within the binding pocket of 4URL. Further, XP-docking pose of compound **15** was overlayed with the MD simulation pose of this compound with an RMSD of 1.23 Å (Supplementary Figure S3). This validates our docking protocol and show the stability of this compound within the catalytic pocket.

The Radius of gyration is indicative of the compaction level, or extendedness of the ligand was found in the range of 4.22 to 5.27 Å (Supplementary Figure S4), indicating the stability of compound **15** within the binding pocket during the MD simulation study. The lower RMSD value (1.28–2.32 Å) during 30 to 150 ns of MD study confirms the less conformational flexibility of compound **15** during MD simulation. The solvent-accessible surface area (SASA) of compound **15** was observed to be in the range of 89.92 to 92.61 $Å^2$, indicating no significant fluctuations in the catalytic pocket residues throughout the MD simulation. In addition, the inhibitor exhibited a low polar surface area (PSA) (111.90 to 138.25 $Å^2$), indicating the complete burial of ligand within the catalytic pocket (Supplementary Figure S5).

We computed binding free energy from the generated 100 trajectory frames of 150 ns MD simulation using the module thermal_mmgbsa.py Script. The average ΔG_{bind} was observed to be -60.35 kcal/mol, which correlates well with the computed MM-GBSA (-63.51 kcal/mol) (Supplementary Figure S6).

Conclusion

HOMO and LUMO values of compound **15** explained that the electronic charge transfer occurred within the system through conjugated paths. The $\Delta E_{HOMO-LUMO}$ of compound **15** was found to be -3.474314 kcal/mol, indicating the kinetic stability of the molecule. Further, MESP studies revealed that the carbonyl oxygen of hydrazide moiety and oxygen atom of phenol ring are the most negative electrostatic potential regions, while nitrogen of the -NH- fragment posses positive electrostatic potential. BDE values represent possible degradation products whose values are greater than 45 kcal/mol. Further, the toxicity profile of degradation products was compared with the compound **15**. Based on the results obtained from docking and free energy studies, it is evident that DPs have less affinity for the binding residues of catalytic pocket compared to the compound **15**. A 150 ns of MD simulation was performed to validate the binding stability of the **15**/4URL

complex. From the results, it is evident that the stability of the ligand was mainly dependent on the interactions with polar and charged residues Gly104, Thr92, Asn49, and Asp52 from the N-terminal domain.

Declarations

Funding

The authors much acknowledge the All India Council of Technical Education (AICTE), National doctoral fellowship (NDF-2018), application number - 56149 for providing the funding support.

Conflict of interest

The authors declare that there are no conflicts of interest in this study.

Availability of data and material

Not applicable

Code availability

Not applicable

Authors contributions

Vidyasrilekha. Yele: Data Curation, Writing, Reviwing and Editing original manuscript; Dilep Kumar. Sigalapalli: Software, Review and editing; Srikanth. Jupudi: Software; Afzal Azam. Mohammed: Conceptualization.

References

[1] R. Wise, T. Hart, O. Cars, M. Streulens, R. Helmuth, P. Huovinen, and M. Sprenger, *Antimicrobial resistance*, British Medical Journal Publishing Group, 1998.

[2] L.L. Silver, *Challenges of antibacterial discovery*, Clinical microbiology reviews 24 (2011), pp. 71-109.

[3] M.A. Fischbach, and C.T. Walsh, *Antibiotics for emerging pathogens*, Science 325 (2009), pp. 1089-1093.

[4] C. Nathan, *Antibiotics at the crossroads*, Nature 431 (2004), pp. 899-902.

[5] J. Davies, and D. Davies, *Origins and evolution of antibiotic resistance*, Microbiology and molecular biology reviews 74 (2010), pp. 417-433.

[6] I. Roca, M. Akova, F. Baquero, J. Carlet, M. Cavaleri, S. Coenen, J. Cohen, D. Findlay, I. Gyssens, and O. Heure, *The global threat of antimicrobial resistance: science for intervention*, New microbes and new infections 6 (2015), pp. 22-29.

[7] C.A. Michael, D. Dominey-Howes, and M. Labbate, *The antimicrobial resistance crisis: causes, consequences, and management*, Frontiers in public health 2 (2014), p. 145.

[8] T. Ertan, I. Yildiz, S. Ozkan, O. Temiz-Arpaci, F. Kaynak, I. Yalcin, E. Aki-Sener, and U. Abbasoglu, *Synthesis and biological evaluation of new N-(2-hydroxy-4 (or 5)-nitro/aminophenyl) benzamides and phenylacetamides as antimicrobial agents*, Bioorganic & medicinal chemistry 15 (2007), pp. 2032-2044.

[9] E. Akı-Şener, K.K. Bingöl, Ö. Temiz-Arpacı, İ. Yalçın, and N. Altanlar, *Synthesis and microbiological activity of some N-(2-hydroxy-4-substitutedphenyl) benzamides, phenylacetamides and furamides as the possible metabolites of*

antimicrobial active benzoxazoles, Il Farmaco 57 (2002), pp. 451-456.

[10] M. Krátký, S. Bősze, Z. Baranyai, J. Stolaříková, and J. Vinšová, *Synthesis and biological evolution of hydrazones derived from 4-(trifluoromethyl) benzohydrazide*, Bioorganic & Medicinal Chemistry Letters 27 (2017), pp. 5185-5189.

[11] S. Bala, G. Uppal, S. Kamboj, V. Saini, and D. Prasad, *Design, characterization, computational studies, and pharmacological evaluation of substituted-N'-[(1E) substituted-phenylmethylidene] benzohydrazide analogs*, Medicinal Chemistry Research 22 (2013), pp. 2755-2767.

[12] V. Raparti, T. Chitre, K. Bothara, V. Kumar, S. Dangre, C. Khachane, S. Gore, and B. Deshmane, *Novel 4-(morpholin-4-yl)-N'-(arylidene) benzohydrazides: synthesis, antimycobacterial activity and QSAR investigations*, European journal of medicinal chemistry 44 (2009), pp. 3954-3960.

[13] H. Lu, X. Zhou, L. Wang, and L. Jin, *Synthesis and Antibacterial Evaluation of N-phenylacetamide Derivatives Containing 4-Arylthiazole Moieties*, Molecules 25 (2020), p. 1772.

[14] Z. Fan, J. Shi, N. Luo, and X. Bao, *Synthesis, crystal structure and antimicrobial activity of 2-((2-(4-(1H-1, 2, 4-triazol-1-yl) phenyl) quinazolin-4-yl) oxy)-N-phenylacetamide derivatives against phytopathogens*, Molecular diversity 23 (2019), pp. 615-624.

[15] S.D. Jorge, M. Ishii, F. Palace-Berl, A.K. Ferreira, P.L. de Sa Junior, A.A. de Oliveira, I.Y. Sonehara, K.F.M. Pasqualoto, and L.C. Tavares, *Preliminary in vitro evaluation of N'-(benzofuroxan-5-yl) methylene benzohydrazide derivatives as potential anti-Trypanosoma cruzi agents*, MedChemComm 3 (2012), pp. 824-828.

[16] T.A. Wani, A.H. Bakheit, A.-R.A. Al-Majed, M.A. Bhat, and S. Zargar, *Study of the interactions of bovine serum albumin with the new anti-inflammatory agent 4-(1, 3-Dioxo-1, 3-dihydro-2H-isoindol-2-yl)-N'-[(4-ethoxy-phenyl) methylidene] benzohydrazide using a multi-spectroscopic approach and molecular docking*, Molecules 22 (2017), p. 1258.

[17] A. Golubović, B. Abramović, M. Šćepanović, M. Grujić-Brojčin, S. Armaković, I. Veljković, B. Babić, Z. Dohčević-Mitrović, and Z.V. Popović, *Improved efficiency of sol–gel synthesized mesoporous anatase nanopowders in photocatalytic degradation of metoprolol*, Materials Research Bulletin 48 (2013), pp. 1363-1371.

[18] R. Ma, B. Wang, S. Lu, Y. Zhang, L. Yin, J. Huang, S. Deng, Y. Wang, and G. Yu, *Characterization of pharmaceutically active compounds in Dongting Lake, China: occurrence, chiral profiling and environmental risk*, Science of the Total Environment 557 (2016), pp. 268-275.

[19] S. Armaković, S. Armaković, N. Finčur, F. Šibul, D. Vione, J. Šetrajčić, and B. Abramović, *Influence of electron acceptors on the kinetics of metoprolol photocatalytic degradation in TiO 2 suspension. A combined experimental and theoretical study*, RSC Advances 5 (2015), pp. 54589-54604.

[20] B. Abramović, S. Kler, D. Šojić, M. Laušević, T. Radović, and D. Vione, *Photocatalytic degradation of metoprolol tartrate in suspensions of two TiO2-based photocatalysts with different surface area. Identification of intermediates and proposal of degradation pathways*, Journal of hazardous materials 198 (2011), pp. 123-132.

[21] M. Blessy, R.D. Patel, P.N. Prajapati, and Y. Agrawal, *Development of forced degradation and stability indicating studies of drugs—A review*, Journal of pharmaceutical analysis 4 (2014), pp. 159-165.

[22] J.J. Molnar, J.R. Agbaba, B.D. Dalmacija, M.T. Klašnja, M.B. Dalmacija, and M.M. Kragulj, *A comparative study of the effects of ozonation and TiO2-catalyzed ozonation on the selected chlorine disinfection by-product precursor content and structure*, Science of the Total Environment 425 (2012), pp. 169-175.

[23] J. Molnar, J. Agbaba, B. Dalmacija, M. Klašnja, M. Watson, and M. Kragulj, *Effects of ozonation and catalytic ozonation on the removal of natural organic matter from groundwater*, Journal of Environmental Engineering 138 (2012), pp. 804-808.

[24] B.S. Mahamuni, A. Jajula, A. Awasthi, P.D. Kalariya, and M.K. Talluri, *Selective separation and characterisation of stress degradation products and process impurities of prucalopride succinate by LC-QTOF-MS/MS*, Journal of Pharmaceutical and Biomedical Analysis 125 (2016), pp. 219-228.

[25] V. Yele, A.A. Mohammed, and A.D. Wadhwani, *Synthesis and Evaluation of Aryl/Heteroaryl Benzohydrazide and Phenylacetamide Derivatives as Broad-Spectrum Antibacterial Agents*, ChemistrySelect 5 (2020), pp. 10581-10587.

[26] —, *Synthesis, Molecular Docking and Biological Evaluation of 2-aryloxy-N-phenylacetamide and N'-(2-aryloxyoxyacetyl) Benzohydrazide Derivatives as Potential Antibacterial Agents*, Chemistry & biodiversity (2021).

[27] M.L. Hall, D.A. Goldfeld, A.D. Bochevarov, and R.A. Friesner, *Localized orbital corrections for the barrier heights in density functional theory*, Journal of chemical theory and computation 5 (2009), pp. 2996-3009.

[28] A.D. Bochevarov, E. Harder, T.F. Hughes, J.R. Greenwood, D.A. Braden, D.M. Philipp, D. Rinaldo, M.D. Halls, J. Zhang, and R.A. Friesner, *Jaguar: A high-performance quantum chemistry software program with strengths in life and materials sciences*, International Journal of Quantum Chemistry 113 (2013), pp. 2110-2142.

[29] A.R. Katritzky, V.S. Lobanov, and M. Karelson, *QSPR: the correlation and quantitative prediction of chemical and physical properties from structure*, Chemical Society Reviews 24 (1995), pp. 279-287.

[30] N.C. Handy, P.E. Maslen, R.D. Amos, J.S. Andrews, C.W. Murray, and G.J. Laming, *The harmonic frequencies of benzene*, Chemical physics letters 197 (1992), pp. 506-515.

[31] R.M. Tovar, K.P. Johnson, K. Ashline, and J.M. Seminario, *Effects of substituents on molecular devices*, International Journal of Quantum Chemistry 108 (2008), pp. 1546-1554.

[32] A. Becke, *A half-half theory of density functionals*, J. Chem. Phys 98 (1993), p. 1372.

[33] S.K. Choubey, R. Mariadasse, S. Rajendran, and J. Jeyaraman, *Identification of novel histone deacetylase 1 inhibitors by combined pharmacophore modeling, 3D-QSAR analysis, in silico screening and Density Functional Theory (DFT) approaches*, Journal of Molecular Structure 1125 (2016), pp. 391-404.

[34] R.A. Friesner, R.B. Murphy, M.P. Repasky, L.L. Frye, J.R. Greenwood, T.A. Halgren, P.C. Sanschagrin, and D.T. Mainz, *Extra precision glide: Docking and scoring incorporating a model of hydrophobic enclosure for protein− ligand complexes*, Journal of medicinal chemistry 49 (2006), pp. 6177-6196.

[35] M.P. Jacobson, D.L. Pincus, C.S. Rapp, T.J. Day, B. Honig, D.E. Shaw, and R.A. Friesner, *A hierarchical approach to all-atom protein loop prediction*, Proteins: Structure, Function, and Bioinformatics 55 (2004), pp. 351-367.

[36] K. Roos, C. Wu, W. Damm, M. Reboul, J.M. Stevenson, C. Lu, M.K. Dahlgren, S. Mondal, W. Chen, and L. Wang, *OPLS3e: Extending force field coverage for drug-like small molecules*, Journal of chemical theory and computation 15 (2019), pp. 1863-1874.

[37] J. Li, R. Abel, K. Zhu, Y. Cao, S. Zhao, and R.A. Friesner, *The VSGB 2.0 model: a next generation energy model for high resolution protein structure modeling*, Proteins: Structure, Function, and Bioinformatics 79 (2011), pp. 2794-2812.

[38] E.M. Duffy, and W.L. Jorgensen, *Prediction of properties from simulations: free energies of solvation in hexadecane, octanol, and water*, Journal of the American Chemical Society 122 (2000), pp. 2878-2888.

[39] C.A. Lipinski, F. Lombardo, B.W. Dominy, and P.J. Feeney, *Experimental and computational approaches to estimate solubility and permeability in drug discovery and development settings*, Advanced drug delivery reviews 23 (1997), pp. 3-25.

[40] W.L. Jorgensen, and J.D. Madura, *Temperature and size dependence for Monte Carlo simulations of TIP4P water*, Molecular Physics 56 (1985), pp. 1381-1392.

[41] C. Lawrence, and J. Skinner, *Flexible TIP4P model for molecular dynamics simulation of liquid water*, Chemical physics letters 372 (2003), pp. 842-847.

[42] U. Essmann, L. Perera, M.L. Berkowitz, T. Darden, H. Lee, and L.G. Pedersen, *A smooth particle mesh Ewald method*, The Journal of chemical physics 103 (1995), pp. 8577-8593.

[43] G.J. Martyna, D.J. Tobias, and M.L. Klein, *Constant pressure molecular dynamics algorithms*, The Journal of chemical physics 101 (1994), pp. 4177-4189.

[44] G.J. Martyna, M.L. Klein, and M. Tuckerman, *Nosé–Hoover chains: The canonical ensemble via continuous dynamics*, The Journal of chemical physics 97 (1992), pp. 2635-2643.

[45] G.J. Martyna, M.E. Tuckerman, D.J. Tobias, and M.L. Klein, *Explicit reversible integrators for extended systems dynamics*, Molecular Physics 87 (1996), pp. 1117-1157.

[46] F.A. Bulat, J.S. Murray, and P. Politzer, *Identifying the most energetic electrons in a molecule: The highest occupied molecular orbital and the average local ionization energy*, Computational and Theoretical Chemistry 1199 (2021), p. 113192.

[47] M. Hida, *Molecular Orbital Consideration of the Reaction of the Zinc-Methylene Complex with Double Bonds*, Bulletin of the Chemical Society of Japan 40 (1967), pp. 2497-2501.

[48] J.S. Murray, P.G. Seybold, and P. Politzer, *The many faces of fluorine: Some noncovalent interactions of fluorine compounds*, The Journal of Chemical Thermodynamics 156 (2021), p. 106382.

[49] P. Sjoberg, J.S. Murray, T. Brinck, and P. Politzer, *Average local ionization energies on the molecular surfaces of aromatic systems as guides to chemical reactivity*, Canadian Journal of Chemistry 68 (1990), pp. 1440-1443.

Figures

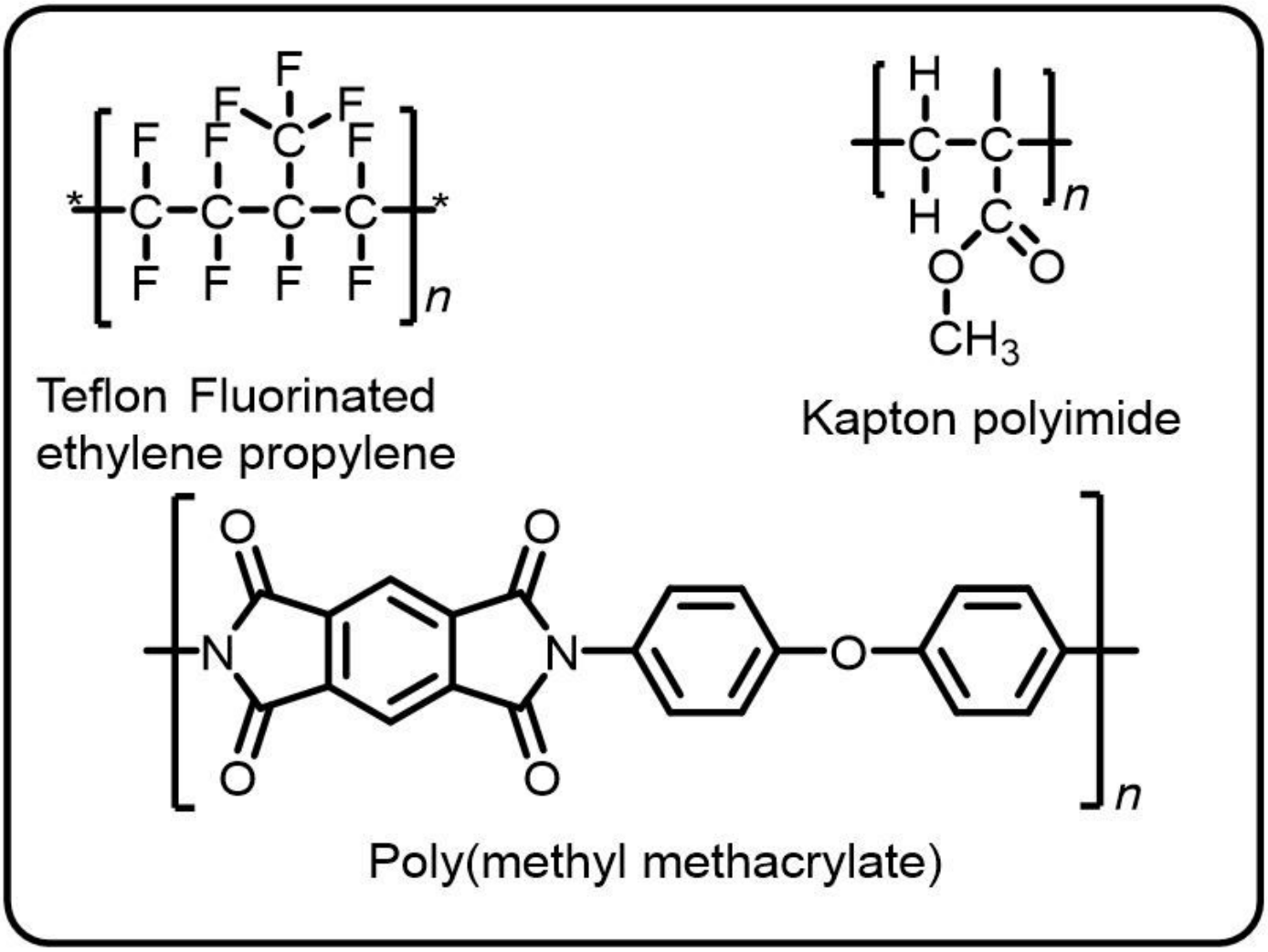

Figure 1

Chemical structures of Teflon Fluorinated ethylene propylene, Kapton polyimide and Poly(methyl methacrylate).

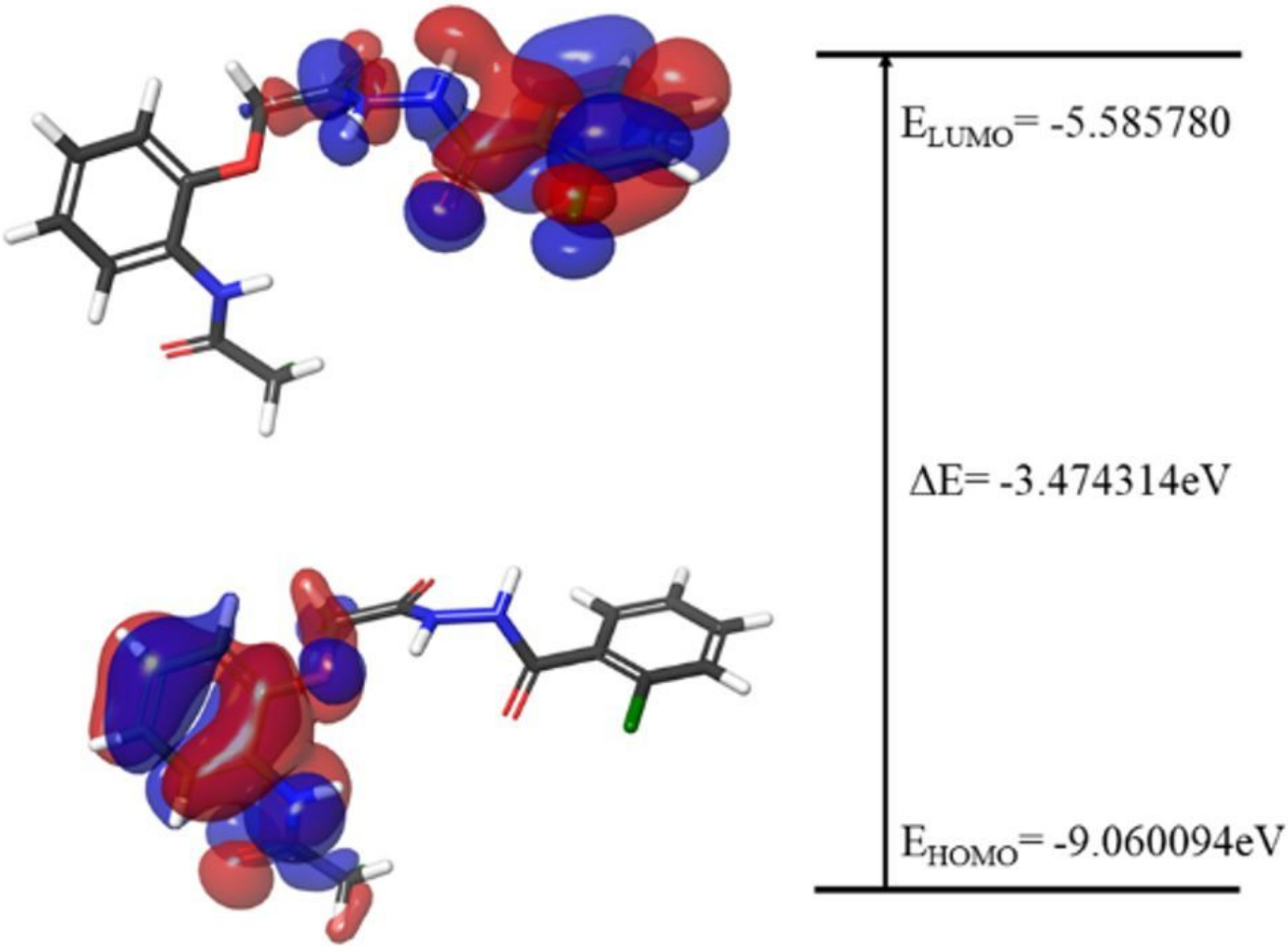

Figure 2

Represent HOMO and LUMO gap of compound 15 obtained using a basis set B3LYP/6-31G**++ with hybrid DFT in the gas phase

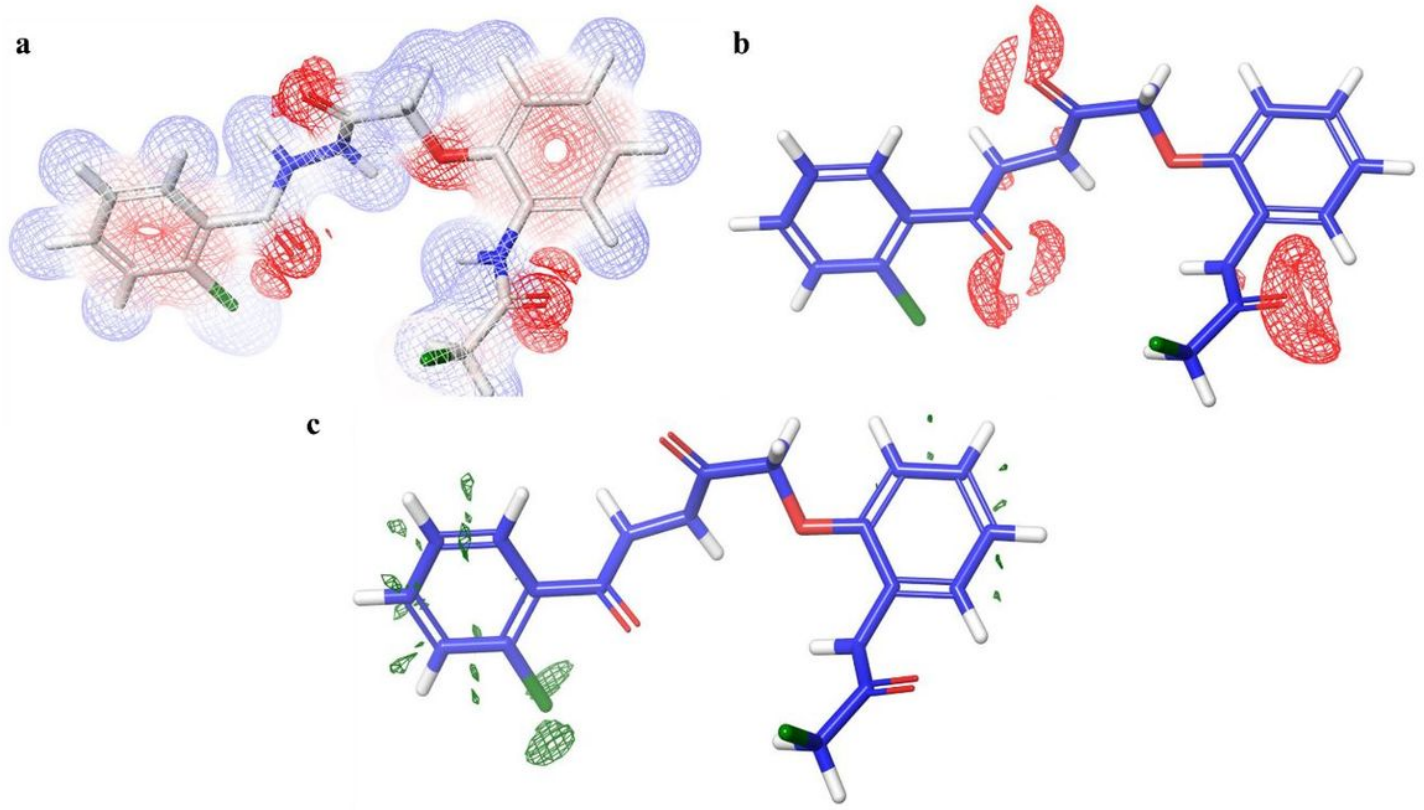

Figure 3

Plots represent (a) Molecular electrostatic potential (MESP) (b) average local ionization energy (ALIE) (c) average local electron affinity (ALEA) of compound 15.

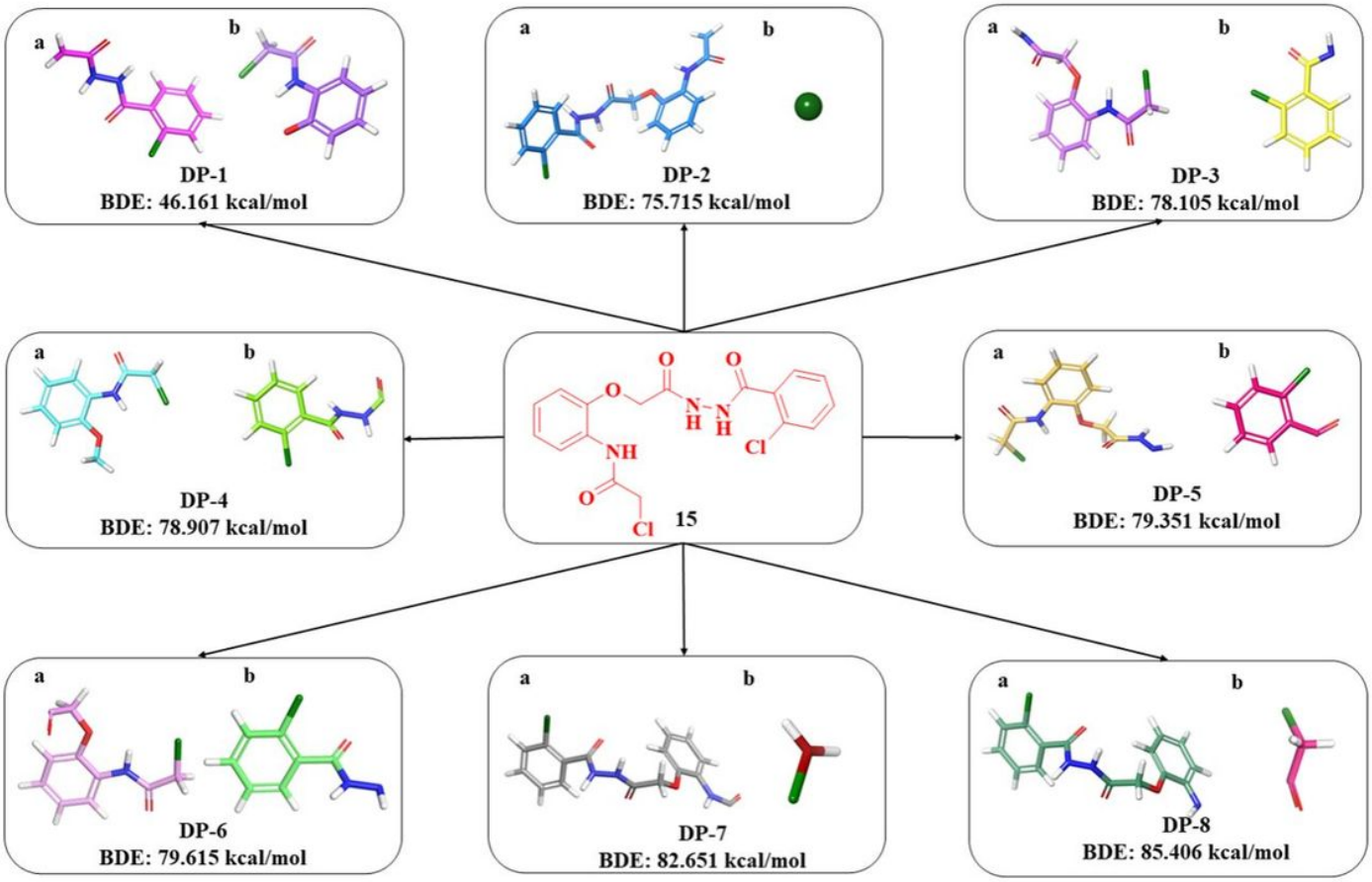

Figure 4

Degradation products/fragments of compound 15 and their bond dissociation energy

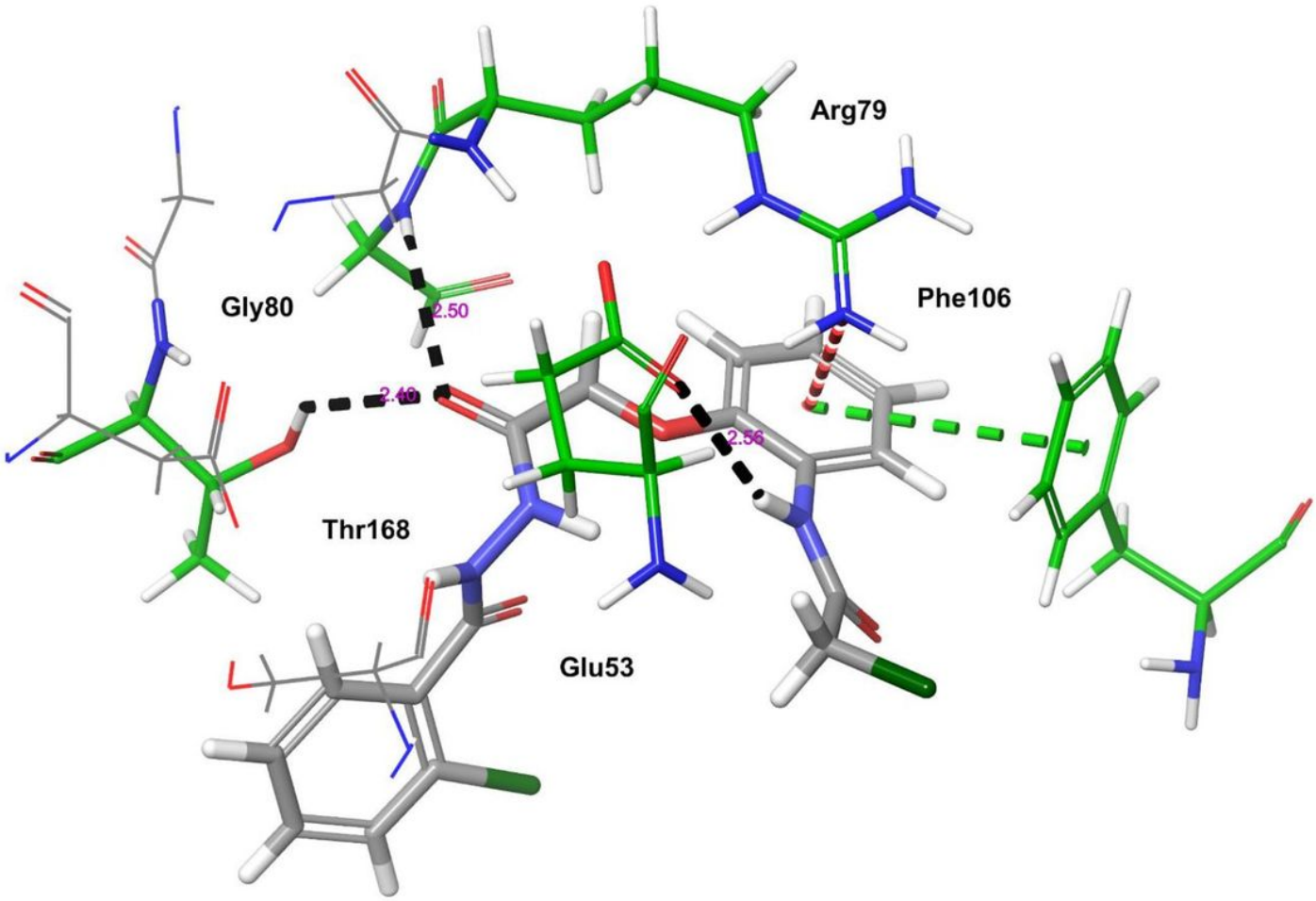

Figure 5

The 3D-interaction diagram compound 15 within the catalytic pocket of S. aureus ParE enzyme

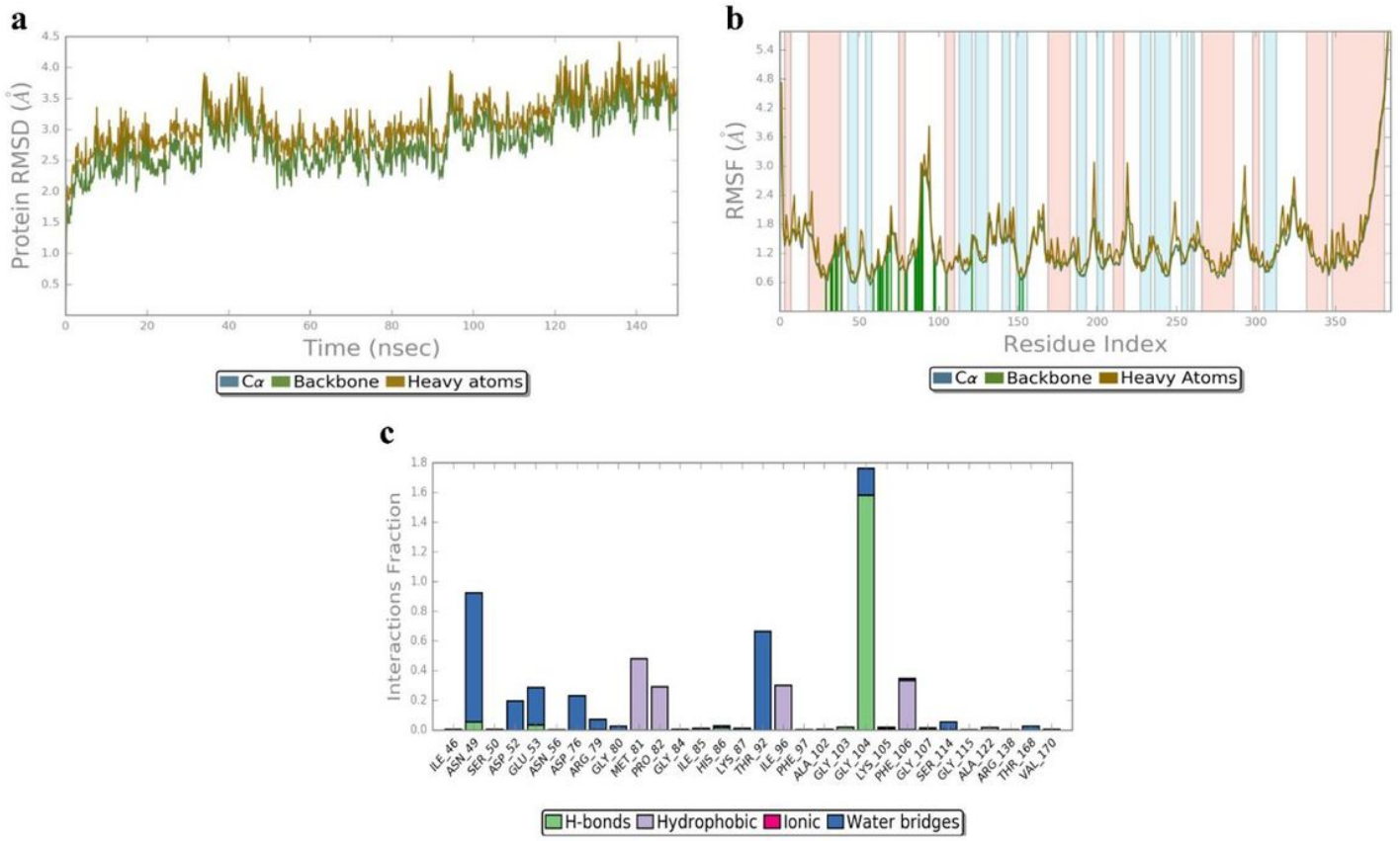

Figure 6

(a) Root mean square deviation (Å) of Cα atoms and backbone (b) Root-mean-square fluctuation profile (c) Interaction profile of complex 15/4URL during 150 ns simulation.

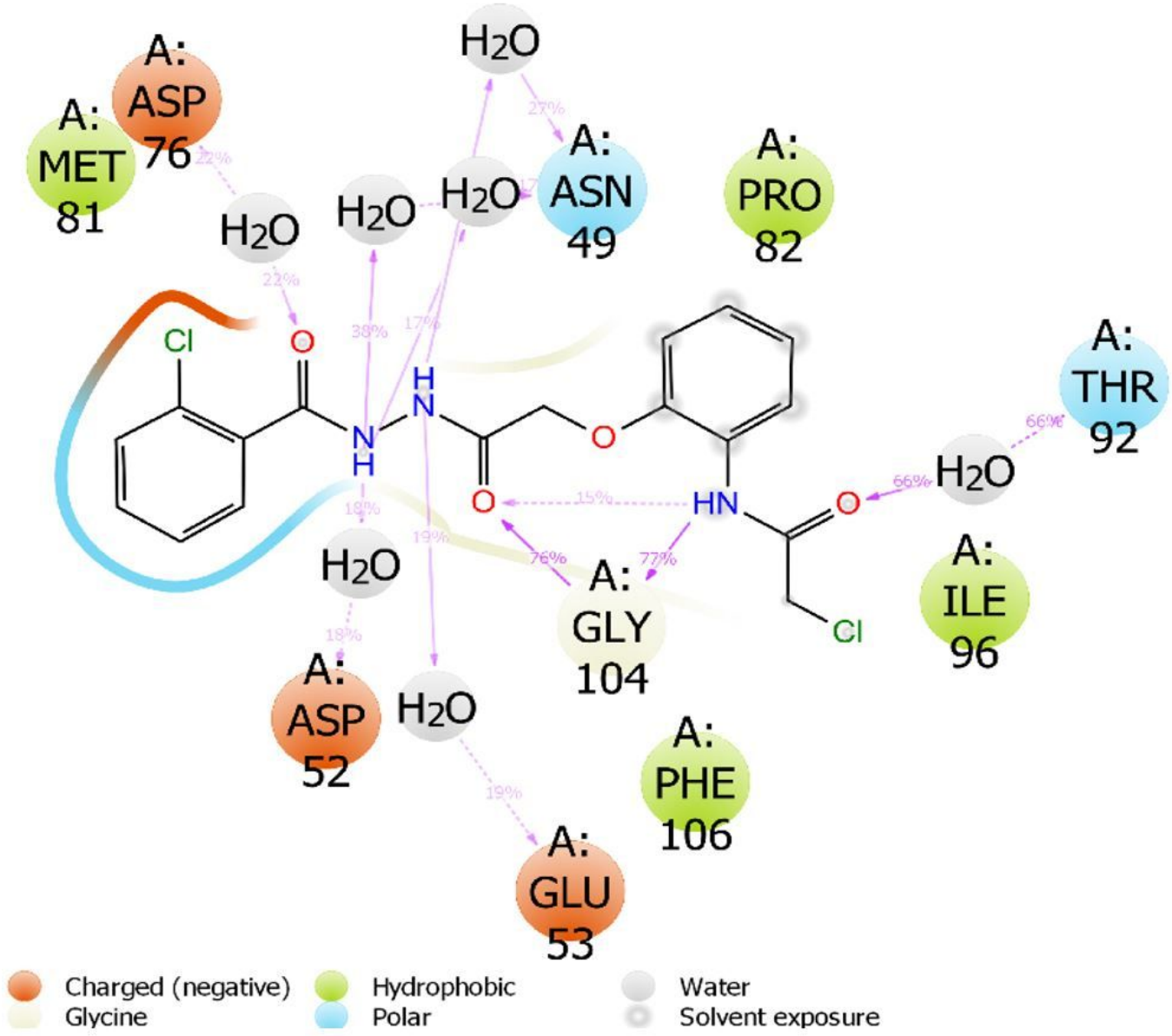

Figure 7

Interaction of compound 15 with different residues of S. aureus ParE enzyme.

Supplementary Files

This is a list of supplementary files associated with this preprint. Click to download.

- SupplementaryInformation.pdf